ARTICLE   OPEN

The interaction of corrosion fatigue and stress-corrosion cracking in a precipitation-hardened martensitic stainless steel

J. Ryan Donahue[1], Amber B. Lass[1] and James T. Burns[1]

Fracture mechanics-based testing was used to quantify the stress-corrosion cracking and corrosion fatigue behavior of a precipitation-hardened martensitic stainless steel (Custom 465-H950) in full immersion chloride-containing environments at two applied electrochemical potentials. A plateau in the cycle-based crack-growth kinetics (da/dN) was observed during fatigue loading at low ΔK and [Cl$^-$] at and above 0.6 M. Evaluation of the fracture morphology and frequency dependence of this plateau behavior revealed an intergranular fracture surface morphology and constant time-dependent growth rates. These data strongly support a controlling stress-corrosion cracking mechanism occurring well below the established K_{ISCC} for quasi-static loading. Low-amplitude cyclic loading below ΔK_{TH} (i.e., "ripple loads") is hypothesized to enable time-dependent intergranular-stress-corrosion cracking to occur below the K_{ISCC} via mechanical rupturing of the crack-tip film and enhancement of the H embrittlement-based SCC mechanism.

INTRODUCTION

Structural integrity management of highly stressed steel components in aqueous chloride environments is a critical engineering challenge with specific applicability to airframe applications.[1–6] The combination of mechanical and corrosion-resistant properties of modern ultra-high-strength stainless steels fulfill the structural design requirements while also eliminating the need for protective platings/coatings that pose environmental and health hazards.[7, 8] Despite these attributes, high-strength steels are highly susceptible to environmental cracking in aqueous chloride environments. Specifically, researchers have demonstrated aqueous chloride environments can: induce localized corrosion damage[9–12] causing a severe reduction in overall fatigue life,[10, 13–21] accelerate fatigue crack-growth rates,[13, 16, 21–27] and enhance susceptibility to stress-corrosion cracking (SCC).[21, 28] Enhancement of the environmental cracking kinetics is widely attributed to hydrogen embrittlement (HE).[24] Recent research on Custom 465, a precipitation-hardened martensitic stainless-steel based on the Fe–Cr–Ni system, quantified and analyzed the corrosion and H-uptake behavior,[29, 30] the pit-to-fatigue crack transition, the short-crack growth and long-crack growth behavior,[13] and the stress-corrosion cracking behavior.[21, 28] Critically, a time-dependent intergranular (IG) fracture process was observed at stress intensity ranges (ΔK) below the threshold value (ΔK_{TH}) during fracture mechanics-based fatigue testing in high [Cl$^-$] environments.[13] Detailed examination of this behavior was outside of the scope of the prior effort but serves as the motivation for the current study.

The concurrent and competing contributions of distinct environmental cracking mechanisms have been recognized to contribute to the total fatigue crack-growth rate. Experimental crack-growth rate data is classically modeled via superposition approaches that aim to decouple these mechanical and environmental influences.[31–34] The premise of such models is that the mechanical and environmental contributions are treated as independent and parallel processes; as such the contribution of each can be independently summed for each loading cycle.[32] In the most basic model, overall measured fatigue crack-growth rate (da/dN) consists of a cycle-dependent rate (da/dN_{cycle}) and a time-dependent rate (da/dN_{time}). Both the pure-mechanical and the corrosion-fatigue contributions comprise the cycle-dependent rate. Creep and (quasi-)static SCC due to portions of the loading cycle exceeding the threshold for stress-corrosion cracking (K_{ISCC}) make up the time-dependent contribution. The relative contributions of each are often scaled according to fractography that identifies the respective areal fraction of the damage morphology. This framework has been used to better understand the impact of various mechanical loading variables (e.g., loading frequency, loading waveform, stress-ratio (R), etc.).[34] However this superposition approach is not fully rigorous due to established, important interactions between mechanical and environmental degradation processes, which are extensively reviewed in the H embrittlement literature.[24, 35, 36] Regardless, this conceptual paradigm offers a reasonable method to decouple and analyse the important contributions of each cracking mechanism.

The objective of the present study is to quantitatively evaluate the effect of bulk [Cl$^-$] on the environmentally enhanced fatigue crack-growth behavior of Custom 465-H950 to elucidate the relative contributions of time-dependent mechanisms and cycle-dependent mechanisms. To this end, the following work was performed: (1) quantitative characterization of SCC and fatigue fracture behavior in various aqueous chloride solutions, (2) systematic investigation of the relative contribution of SCC and corrosion fatigue to overall crack-growth behavior, and (3) discussion of the implications of obtained results in the context of engineering applications.

[1]Department of Materials Science and Engineering, University of Virginia, Charlottesville, VA 22904, USA
Correspondence: James T. Burns (jtb5r@virginia.edu)

np**j**

The interaction of corrosion fatigue and SCC
JR Donahue et al.

2

RESULTS

The stress-corrosion crack-growth rates (da/dt) vs. stress intensity (K) relationship for C465-H950 polarized to −550 mV$_{SCE}$ in 0.6 M NaCl solution is shown in Fig. 1.[28] The apparent increasing da/dt for $K < 75$ MPa$\sqrt{m}$ is not real crack extension and rather is due to an effect of crack-tip plasticity on the electrical resistivity. This behavior leads to a false increase of the measured potential that the direct current potential difference (dcPD) method translates into an indication of crack extension.[37] This behavior is the basis of for the plotted resolution limit reported in Fig. 1, which was previously established using C465 and other UHSS data (Pioszak, G. Unpublished work, University of Virginia, 2013).[28] Stage I cracking occurs above the K_{ISCC} of ≈75 MPa$\sqrt{m}$ as typified by a rapid increase in da/dt with increasing K. A plateau in da/dt (stage II behavior; da/dt_{II}) is observed at ≈10^{-5} mm/s from roughly 120–160 MPa$\sqrt{m}$. Further increase in K results in a rapid increase in growth rate as the K approaches and exceeds the critical stress intensity for fracture. Although the plane strain fracture toughness (K_{IC}) for this C465-H950 has been reported to be 95 MPa$\sqrt{m}$, failure at stress intensities exceeding K_{IC} are reasonable considering the lack of pure plane strain conditions in the single edge notch (SEN) sample. Fractography in Fig. 2 (cracking from right to left) confirms the presence of intergranular-stress-corrosion cracking (IG-SCC) for the slow-rising K testing protocol. Critically, identical testing at −200 mV$_{SCE}$ in 0.6 M NaCl (not reported here) did not result in IG-SCC crack growth that exceeded the resolution limit.

The da/dN vs. ΔK relationship for C465-H950 is shown in Fig. 3 for the K-shed protocol at $f = 2$ Hz and in humid N$_2$, and various aqueous NaCl electrolytes polarized to −200 and −550 (0.6 M NaCl only) mV$_{SCE}$. In general, the humid N$_2$ and 0.0006–0.06 M NaCl results are tightly clustered with the humid N$_2$ growth rates being marginally lower and the apparent threshold values being in the range of 3.7–4.3 MPa$\sqrt{m}$. Consistent with a companion study of this material lot (at constant R of 0.5), the growth rates do not scale with increasing NaCl over this concentration range.[13] Critically, the deionized (DI) water and 0.6 M NaCl results deviate from these data trends. Specifically, the growth rates measured in 0.6 M NaCl tests at −200 and −550 mV$_{SCE}$ are well aligned with the lower concentration results for Δ$K > 6.6$ and 8.2 MPa$\sqrt{m}$, respectively, but at lower ΔK deviate to a constant da/dN of ≈8×10^{-5} and 3×10^{-5} mm/cycle, respectively. This plateau in da/dN

continues until the test was concluded at a ΔK of 2.5 MPa$\sqrt{m}$ (or a K_{max} of 5 MPa$\sqrt{m}$). Similar behavior is observed for the DI water test, however, growth rates are slightly higher than the cluster of NaCl results. Specifically, the growth rates deviate from the cluster at a higher ΔK of ≈12 MPa$\sqrt{m}$ and rise to a higher plateau value of da/dN (≈1.5×10^{-3} mm/cycle). This seemingly anomalous behavior in ostensibly less severe DI water is consistent with prior findings of enhanced SCC in pure water and low chloride concentrations.[38, 39] Researchers postulate that this behavior could correlate to extrinsic toughening due to local branching in the higher chloride conditions; however, this argument is not fully satisfying.[39] Detailed investigation of the mechanistic cause of this behavior is outside the scope of this study.

Representative fractography from the fatigue specimens are presented in Fig. 4. An overview of the fracture surface of 0.06 M NaCl test is presented in Fig. 4a, which shows the notch, pre-crack region, area of constant K_{max} fatigue testing, and final fracture. The red lines denote the crack depths at the transition points for each regime, as gathered from dcPD readings of crack length. The

Fig. 2 Fractography of Custom 465-H950 tested at using slow-rising displacement of 0.0003 mm/min (corresponding to a dK/dt of ~1 MPa$\sqrt{m}$/h prior to the onset of cracking) in 0.6 M NaCl at −500 mV$_{SCE}$. Lines delineate the transition between the indicated regions of the specimen/test
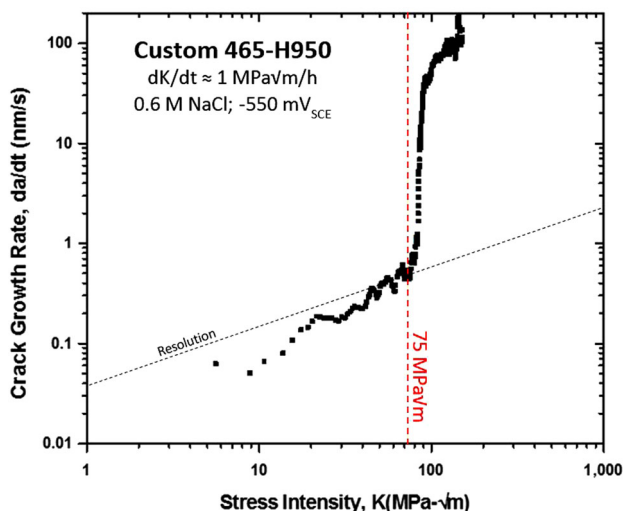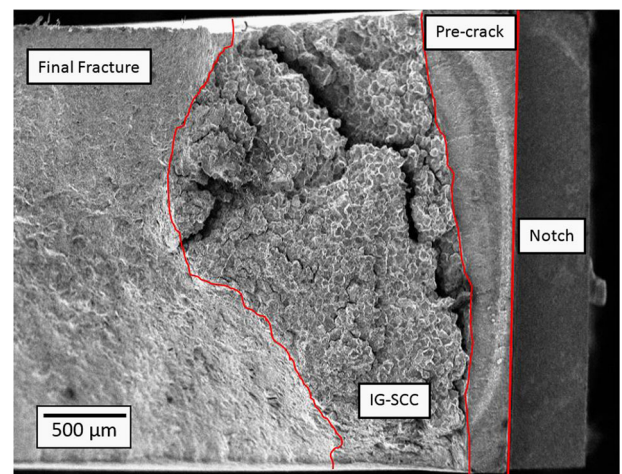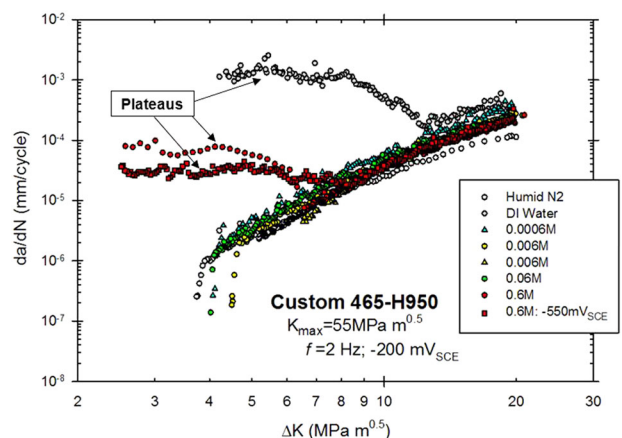

Fig. 1 Stress-corrosion cracking rate vs. stress intensity for Custom 465-H950 tested at using slow-rising displacement of 0.0003 mm/min (corresponding to a dK/dt of ≈1 MPa$\sqrt{m}$/h prior to the onset of cracking) in 0.6 M NaCl at −550 mV$_{SCE}$, dotted line is the plasticity induced resolution limit for the dcPD testing method

Fig. 3 Fatigue crack-growth rate vs. stress intensity range for Custom 465-H950 tested under a constant K_{max} (55 MPa$\sqrt{m}$)-decreasing ΔK at a frequency of 2 Hz in humid nitrogen gas (RH > 90%), deionized water, and NaCl concentrations ranging from 0.0006–0.6 M at either −200 or −550 mV$_{SCE}$
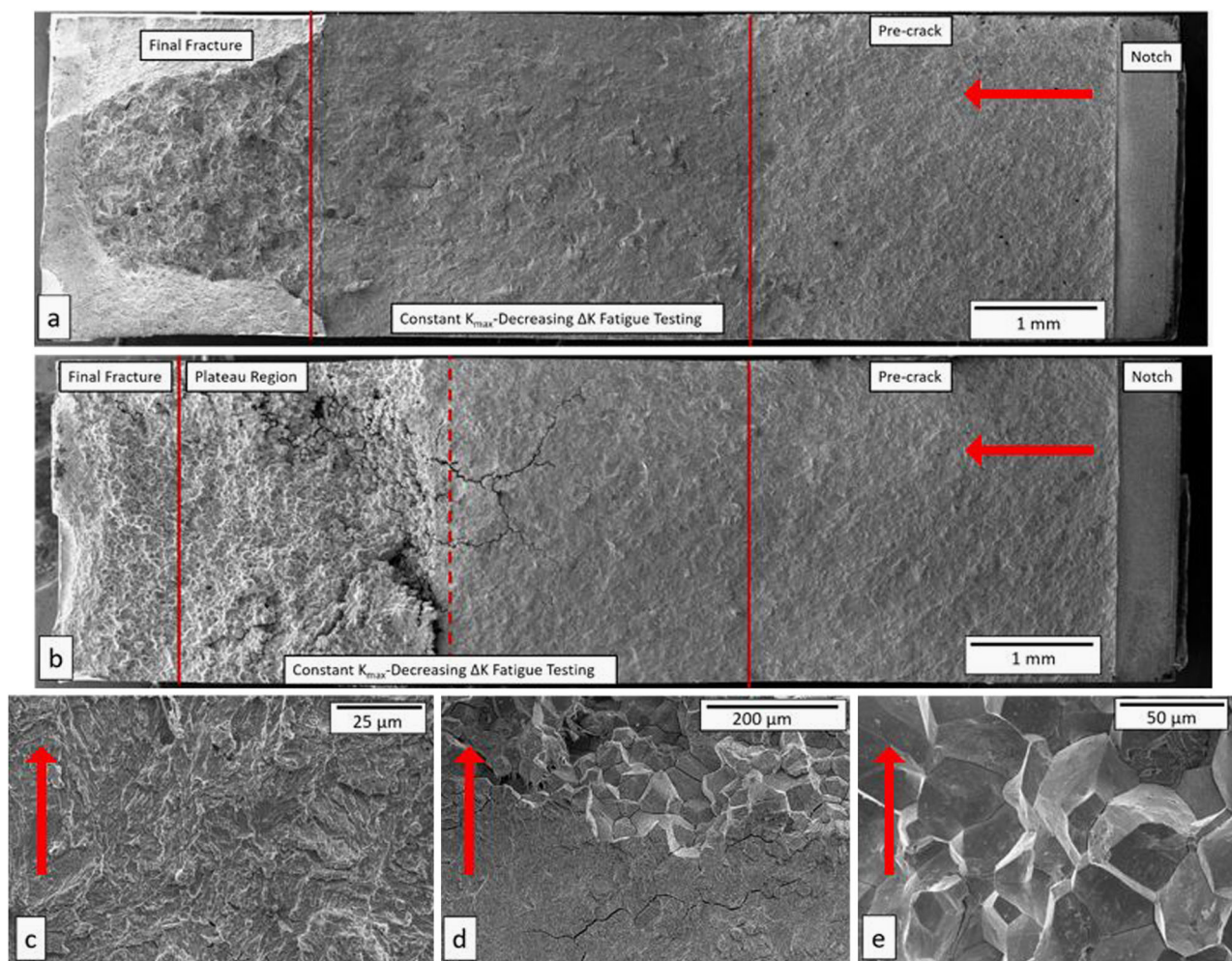
The interaction of corrosion fatigue and SCC
JR Donahue et al.

npj

3

Fig. 4 Fractography of Custom 465-H950 tested under K-shed protocol at a potential of -200 mV$_{SCE}$ in 0.06 M NaCl **a**, **c** and 0.6 M NaCl **b**, **d**, **e**. Crack-growth direction in **a**, **b** is right to left and in **c**, **d**, **e** is from bottom to top as indicated by the *red arrows*. *Lines* in **a**, **b** indicate the dcPD indicated crack lengths associated with the transitions in fatigue behavior in Fig. 3

region of constant K_{max} cracking shows a transgranular morphology (Fig. 4c) that is consistent with the previously reported morphology for this material in NaCl environments.[13] This morphology transitions to a ductile microvoid appearance during final fracture. No significant differences are observed between fracture surfaces of each test in the range of 0.0006–0.06 M NaCl at -200 mV$_{SCE}$. Figure 4b is an overview of the higher [Cl$^-$] (0.6 M NaCl test at -200 mV$_{SCE}$), where there is a similar transgranular morphology (Fig. 4d, lower portion) that then transitions to an IG morphology (Fig. 4d, top portion and Fig. 4e). This morphology transition directly aligns with the dcPD-based crack length (*dotted line* in Fig. 4b) at the onset of the plateau region in Fig. 3. This morphology progression is observed for each of the tests, where the elevated plateau behavior is observed at low ΔK.

DISCUSSION

The SCC and fatigue data for C465-H950 in NaCl environments in Figs. 1–4 raise two critical questions. First, is the plateau in fatigue crack-growth rates (Fig. 3) that exhibits an IG cracking morphology (Fig. 4b, e) caused by the onset of a SCC-based, time-dependent cracking mechanism? The plateau behavior in Fig. 3 typifies the "Type B" corrosion fatigue behavior classically proposed by McEvily and Wei,[34] where the contribution of time (not cycle)-dependent cracking dominates. However, the unique aspect of the current data is that the crack initiates and persists well below

the K_{ISCC}; this motivates the second question. If this behavior is an IG-SCC mechanism, what facilitates the onset of time-dependent cracking below the K_{ISCC} threshold (≈ 75 MPa$\sqrt{m}$, Fig. 1) established via fracture mechanics-based slow-rising displacement testing?

Evidence supporting an IG-SCC mechanism

There are three primary findings that support an IG-SCC-based mechanism as the root cause for the growth rate plateaus at low ΔK. First, fracture surface images in Fig. 4 (and in prior work[13]) demonstrate that environment-enhanced fatigue typically results in a transgranular fracture morphology. As such, direct correlation between the onset of the IG morphology and the plateau growth rates suggests a change in mechanism. Although this correlation is convincing, the coupled increase in growth rates and IG morphology does not conclusively establish a change to a time-dependent SCC mechanism. Specifically, this IG morphology could still be controlled by the cycle-dependent plastic damage accumulation, where the transgranular to IG transition is caused by a shift in the critical localization of the damage accumulation to proximate to the grain boundaries. Although unlikely, this scenario precludes a definitive conclusion based solely on the fractography.

Second, to investigate the relative importance of time- and cycle-dependent damage mechanisms, the K-shed experiments are repeated in 0.6 and 1.5 M NaCl at -200 mV$_{SCE}$. These tests are
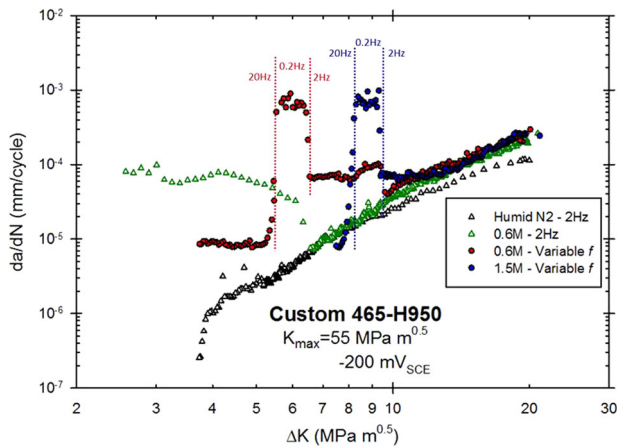
npj

The interaction of corrosion fatigue and SCC
JR Donahue et al.

4

Fig. 5 Fatigue crack-growth rate vs. stress intensity range for Custom 465-H950 tested under a constant K_{max} (55 MPa$\sqrt{m}$)-decreasing ΔK in humid nitrogen gas (RH > 90%) and 0.6/1.5 M NaCl at −200 mV$_{SCE}$. Lines indicate points at which the frequency was changed to the indicated values

conducted in the same manner as those reported in Fig. 3, however once the plateau growth rates are observed the frequency is varied from 2 to 0.2 Hz, then to 20 Hz. Critically, if this is a truly time-dependent cracking mechanisms (i.e., da/dt is constant) then varying frequency should result in an inversely proportional change in the cycle-based cracking rate as captured by the relationship in Eq. 1

$$\frac{da}{dN} = \frac{1}{f} \times \frac{da}{dt} \qquad (1)$$

Such a relationship is observed at both 0.6 (red circle) and 1.5 M (blue circle) NaCl environments in Fig. 5, where the humid N$_2$ (open black triangle) and 0.6 M NaCl (open red triangle) results from Fig. 3 are reproduced. The initial 2 Hz portion of the variable frequency tests show the onset of a plateau in da/dN at ΔK of ≈10 and 13 MPa$\sqrt{m}$ for 0.6 and 1.5 M NaCl, respectively. The onset of the plateau occurs at slightly higher ΔK values as compared to the constant frequency test 0.6 M test (6.6 MPa$\sqrt{m}$), however, the plateau growth rates are nearly equivalent for all tests (≈8 × 10^{-5} mm/cycle). Critically, changing testing frequency from 2 to 0.2 Hz (at 9.5 and 6.5 MPa$\sqrt{m}$, for 0.6 and 1.5 M, respectively) the da/dN value increased by an order of magnitude to ≈8 × 10^{-4} mm/cycle. A subsequent increase in the frequency to 20 Hz, resulted in a reduction of the da/dN to ≈8 × 10^{-6} mm/cycle. Following Eq. 1, these frequency-dependent changes in da/dN suggest a constant da/dt (≈4 × 10^{-5} mm/s) and strongly support a governing role of a time-dependent cracking mechanism.

Third, for each testing environment, the magnitude of the da/dt value (calculated via Eq. 1) in the plateau regime is constant over a wide range of low ΔK values. This is consistent with the dominant role of the constant K_{max} in SCC and opposed to a mechanism controlled by cyclic-damage accumulation (which would result in a growth rate dependence on ΔK). Furthermore, the time-dependent growth rates for the 0.6 M NaCl and −550 mV$_{SCE}$ environment gathered from slow-rising displacement testing (Fig. 1; da/dt_{II} ≈1 × 10^{-5} mm/s) and fatigue testing (Fig. 3; ≈1.5×10^{-5} mm/s) are remarkably similar. This similarity is consistent with a HE-based SCC mechanism, where crack growth in the Stage II regime is proposed to be rate limited by diffusion of H ahead of the crack tip.[37, 40–42] Specifically, if the HE-based SCC mechanism is controlling and if there is a constant crack-tip environment to set equivalent H production rates, then these equivalent growth rates would be expected due to constant diffusion rates in the crack-tip process zone. In toto, the IG fracture morphology, frequency dependence, and da/dt values strongly support a SCC-
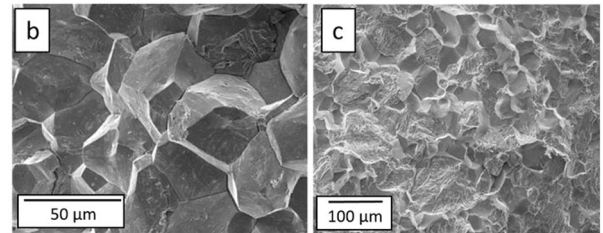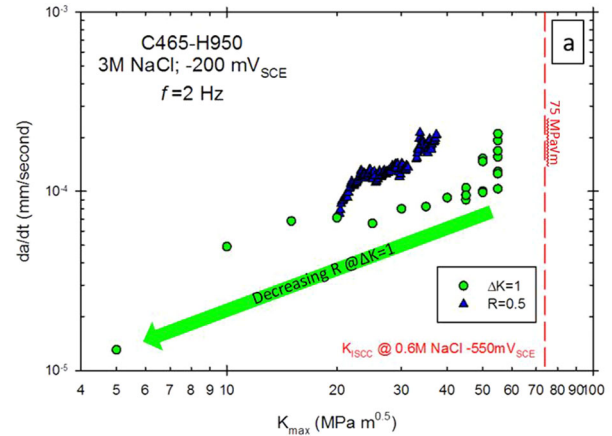

Fig. 6 Time-based crack-growth rates vs. maximum stress intensity **a** for Custom 465-H950 tested at a frequency of 2 Hz in 3 M NaCl at −200 mV$_{SCE}$. Data and fractography is reported for a loading protocol, where there is a constant applied ΔK (circles and **b**) or at a constant cyclic stress range at $R = 0.5$ (triangles and **c**)

based mechanism governing the plateau behavior observed at low ΔK.

IG-SCC below the K_{ISCC}

Cyclic-loading contribution to IG-SCC susceptibility: evidence. Although the evidence strongly suggests that the plateau in da/dN at low ΔK values (Fig. 3) is due to a time-based IG-SCC cracking mechanism, it is critical to understand why IG-SCC occurs at unexpectedly low K_{max} values. Sub-K_{ISCC} cracking is directly demonstrated for (1) 0.6 M NaCl at −550 mV$_{SCE}$ in Fig. 3, where cracking occurs well below the K_{ISCC} of ≈75 MPa$\sqrt{m}$ (Fig. 1) and (2) 0.6 M NaCl at −200 mV$_{SCE}$, where no IG-SCC cracking was observed in slow-rising displacement testing.

The data were also augmented by two sets of additional tests in 3 M NaCl at −200 mV$_{SCE}$ at a frequency of 2 Hz (Fig. 6). In the first experiment (green circles), the specimen is pre-cracked then cyclically loaded at various K_{max} values ranging from 55 to 5 MPa$\sqrt{m}$, while keeping a constant ΔK of 1 MPa$\sqrt{m}$ (correspondingly, R ranged from 0.98 to 0.8). At each K_{max} value, cyclic loading continued until a steady state growth rate was achieved. Once a da/dt was established at a given K_{max} the test is paused, the K_{max} was decremented by 5 MPa$\sqrt{m}$, and then the test was resumed at the lower K_{max} value. After the initial descent from K_{max} of 55 to 5 MPa$\sqrt{m}$, isolated replicates at intermediate K_{max} values were performed to establish that there were no complicating effects of load history or crack length. The data (Fig. 6a) at a $\Delta K = 1$ MPa$\sqrt{m}$ show scatter in da/dt from 1–2 × 10^{-4} mm/s at a K_{max} of 55 MPa$\sqrt{m}$. A marginal decrease in da/dt from 1 × 10^{-4} to 6.5 × 10^{-5} mm/s is observed as the K_{max} is decreased from 55 to 15 MPa$\sqrt{m}$, followed by a more significant decrease to 1.3 × 10^{-5} mm/s as K_{max} falls to 5 MPa$\sqrt{m}$. For all K_{max} levels, the fracture surface exhibits a purely IG morphology (Fig. 6b), consistent with an IG-SCC-based mechanism. Critically, despite the slower da/dt values at lower K_{max} values, continued IG-SCC cracking is observed at K_{max} values as low as 5 MPa$\sqrt{m}$, well below K_{ISCC}.

The interaction of corrosion fatigue and SCC
JR Donahue et al.

npj

5

In the second experiment (*blue triangles*), the specimen was cracked from the notch at a constant maximum stress of 300 MPa and an R of 0.5. Data are only reported for crack lengths above 1 mm, where an influence of the machined notch is not expected.[13] The resulting data are plotted as da/dt (converted from da/dN via Eq. 1) vs. K_{max} (Fig. 6a). Data from the $R = 0.5$ test show a sharp increase in growth rate from K_{max} of 20 to 23 MPa$\sqrt{m}$, which is consistent with a fatigue threshold regime at ΔK of 10 MPa$\sqrt{m}$ observed for identical $R = 0.5$, K-rising testing of this lot of Custom 465-H950 in a related study.[13] This is followed by a slow increase in da/dt from 1×10^{-4} to 2×10^{-4} mm/s as K_{max} increased from 23 to 39 MPa$\sqrt{m}$. Fractography taken at ≈ 25 MPa$\sqrt{m}$ demonstrates a mixed IG and transgranular morphology. Such morphology is observed over the entire fracture surface, suggesting that the pure IG-SCC (*green circles*) mechanism is augmented by a cycle-based, transgranular fatigue mechanism for the higher stress ranges (*blue triangles*) associated with the $R = 0.5$ loading. The coupled IG-SCC and transgranular fatigue contribution is consistent with the higher observed growth rates as compared with the $\Delta K = 1$ MPa$\sqrt{m}$ data and the superposition model of time-dependent crack growth and cycle-dependent crack-growth contributions proposed by Wei.[32] These data clearly demonstrate that (1) small scale, sub-threshold cyclic loading ($\Delta K = 1$ MPa$\sqrt{m}$) can cause time-dependent pure IG-SCC cracking, and (2) cyclic loading above threshold at $R = 0.5$ results in a mix of transgranular cracking governed by cyclic-damage accumulation and time-dependent IG-SCC. Critically, these data suggest that cyclic loading (even at low amplitudes) will enable the onset of IG-SCC at K_{max} values as low as 5 MPa$\sqrt{m}$ in a 3 M NaCl environment.

A systematic fracture mechanics-based evaluation (e.g., Fig. 1) of the effect of chloride concentration on the IG-SCC behavior is needed but outside the scope of the current study. As changes in bulk chloride concentration, heat treatment, and applied electrochemical potential can critically influence the K_{ISCC}, it is important to evaluate literature K_{ISCC} values to ensure that comparisons to the current data are justified. Vasudevan and colleagues[21] used rising step load data to demonstrate that varying chloride concentration from 0.0006 to 0.6 M will substantially alter the IG-SCC susceptibility of Custom 465 (60% cold worked then aged for 4 h at 551 °C). This finding is consistent with the lack of IG-SCC observed below 0.6 M NaCl in Fig. 3. However, abundant evidence supports the development of an aggressive, occluded, high [Cl⁻] crack-tip environment (particularly in Cr-containing steels),[27, 43–47] suggesting a secondary influence of increasing bulk chloride content above a critical level necessary for the onset of IG-SCC. Specifically, increasing bulk chloride concentration from 0.6 to 3 M NaCl will have minimal effect due to the development of a constant, occluded crack-tip environment (for H production) and crack-growth limitation by H-diffusion in the process zone. This is consistent with the data that show similar da/dt values (ranging from $1–4 \times 10^{-5}$ mm/s) for areas that exhibit pure IG-SCC at 0.6 (both at −200 and −550 mV$_{SCE}$), 1.5, and 3 M NaCl. Andresen et al.[47] propose that such an aggressive occluded environment can develop even in very low bulk chloride solutions. As such, both the lack of IG-SCC behavior at low chloride concentrations and the IG-SCC-like behavior in DI water require further investigation. Regardless, these data suggest that the increase in bulk chloride concentration to 3 M is unlikely to reduce K_{ISCC} sufficiently to be responsible for the cracking observed at 5 MPa$\sqrt{m}$ (Fig. 6a).

Furthermore, prior fracture mechanics testing of the current lot of Custom 465 in the H900 condition (higher strength and more susceptible to IG-SCC[21]) at polarizations between −500 and −250 mV$_{SCE}$ in 0.6 M NaCl show a lower bound K_{ISCC} value of 47 MPa$\sqrt{m}$ with some specimens demonstrating immunity.[28] This value fell to ≈ 10 MPa$\sqrt{m}$ for cathodic polarizations <−500 mV$_{SCE}$ and at an anodic polarization of −150 mV$_{SCE}$ (open circuit poential (OCP) was measured at −225 mV$_{SCE}$). The strong dependence on applied electrochemical potential is recognized, however, the importance of cyclic loading (apart from the effect of applied potential) on IG-SCC is supported by two findings. First, given the enhanced susceptibility of the H900 condition compared to H950 (as shown for Custom 465 (ref. [21]) and for a similar precipitation-hardened martensitic steel, Ferrium PH48S[28, 48]), the K_{ISCC} values reported for the H900 condition can be considered lower bounds for the H950 used in the current study. Second, even at the most aggressive polarizations on the more susceptible H900 condition, the K_{ISCC} of ≈ 10 MPa$\sqrt{m}$ is still greater than K_{max} of ≈ 5 MPa$\sqrt{m}$, where IG was observed in Figs. 3, 5 and 6.

In toto, the data and arguments above demonstrate that cyclic loading (even at low amplitudes) enable IG-SCC at a K_{max} well below the K_{ISCC} established using fracture mechanics-based SCC testing approaches. Detailed mechanistic interpretation is necessary to understand what aspect of the mechanistic IG-SCC process is influenced by low level cyclic loading to enable this behavior.

Cyclic-loading contribution to IG-SCC susceptibility: mechanisms. The effect of small-amplitude load perturbations, known as ripple loads, superimposed on a constant stress has been previously shown to induce fracture at stress intensity levels below K_{ISCC}.[49–54] Such behavior breaches two traditional crack-growth thresholds: (1) the fatigue ΔK_{TH}, which is the threshold for cyclically induced plasticity (potentially lowered by internal or environmental H embrittlement), and (2) the K_{ISCC} for monotonic/quasi-static time-dependent cracking. Bayles et al.[54] use results from high mean stress and low ΔK experiments to argue for a novel environmental damage mechanism caused by cyclic loading that enables traditional time-dependent SCC. This hypothesis is challenged by Gangloff[42] and Horstmann et al.[55] who suggest that this behavior is more simply described as an environment-enhanced cycle-based process. They contend that confusion arises simply from challenges in establishing the intrinsic threshold for fatigue-crack propagation in the relevant environment. The systematic testing protocol presented above addresses the experimental shortcomings identified by Gangloff/Horstmann. Critically, the cyclic loading-induced, time-dependent SCC behavior persists, warranting commentary on the mechanistic cause for this behavior. Cyclic loading may induce the onset of true time-dependent IG-SCC behavior by (1) changes in the local chemistry that enhance the local H production at the crack tip, and/or (2) mechanically damaging a protective crack-tip film, thereby enabling enhanced H uptake.

Cyclically induced crack-chemistry changes: If crack chemistry is responsible for IG-SCC at a K_{max} well below K_{ISCC}, then cyclic loading must induce a more aggressive occluded crack-tip environment than would be present for a (quasi-)statically loaded crack, typical of the slow-rising displacement test in Fig. 1. Critically, the development of an occluded crack-tip chemistry compositionally distinct from the bulk environment is central to understand the environmental cracking phenomena.[56] For stainless steels in aqueous chloride electrolytes, the continuous rupturing of the crack-tip passive film exposes bare underlying metal and enables local dissolution. Subsequent deaeration and hydrolysis of ferrous and Cr³⁺ cations will reduce the crack-tip pH and will require/result in an influx of anions to maintain electroneutrality. Critically, this process (akin to crevice corrosion) is predicated on the fact that there is limited transport between the bulk and the crack tip due to the narrow crack-wake channel.[13] Under cyclic loading, Turnbull has established that the formation and retention of occluded crack-tip chemistry will depend on two components: (1) diffusion-based flow governed by gradients in composition and ion migration, and (2) convective mixing (or bulk fluid flow) caused by the undulating motion of the crack flanks.[57, 58]

Concerning the diffusion-based flow, higher bulk [Cl⁻] would lead to a weaker ionic concentration gradient between the crack

npj

The interaction of corrosion fatigue and SCC
JR Donahue et al.

6

tip to the bulk and thus potentially slow the dilution of the aggressive crack-tip environment. Although this would reasonably correlate with the observation of IG-SCC at higher bulk [Cl⁻], it does not provide insight into why IG-SCC is promoted by low level cyclic loads. Assuming a trapezoidal crack Turnbull developed the following equation for the critical crack depth (l_{crit}) below which diffusion-based flow is dominant

$$l_{crit} = \frac{\sqrt{D/f}}{1 - \sqrt{R}} \qquad (2)$$

where D is the diffusion coefficient of the dissolved species in the crack-tip solution.[57] The critical crack depth is exceeded in all cases, where IG-SCC behavior is observed in this study, suggesting that convective mixing dominates crack-tip chemistry kinetics, whereas diffusion contributions are secondary. Convective mixing during cyclic loading could either (1) serve to dilute the aggressive (low pH and high [Cl⁻]) crack-tip solution by enhanced mixing with the bulk environment, and/or (2) enable enhanced oxygen ingress.[27] Either of these would reduce the propensity for time-dependent IG-SCC. Furthermore, in the context of the K-shed experiments, the R is constantly decreasing as the ΔK falls and crack length increases, leading to enhanced convective mixing.[42, 57] As such, although changes in crack depth/geometry and loading have an important influence on the crack chemistry, crack depth-dependent changes in crack chemistry cannot reasonably explain the onset of and continued IG-SCC behavior at intermediate to low ΔK values (Fig. 3). In toto, crack-chemistry arguments cannot adequately explain the observed increase at time-dependent IG crack growth that is triggered by low level cyclic loading.

Cyclically induced crack-tip film rupture: H generation and uptake are vastly accelerated at bare-metal surfaces as compared to those with stable films.[59, 60] As such, in the HE paradigm, severe time-dependent IG-SCC is often predicated on the crack-tip environment being sufficiently aggressive to fully/partially defect the passive film and enable the underlying bare metal to come into contact with its surrounding environment.[61] For non-cyclic loading, many researchers have noted that the crack-tip strain rate associated with active increase in loading, creep, or crack advance will augment the pure electrochemical effects on the film stability.[24, 50, 51, 59, 61–64] The concept of cyclic loading-induced rupture of a crack-tip protective film that enables HE (or other environmentally induced processes) has been postulated to explain how loading frequency and corrosion inhibitors influence various alloy-environment systems, which contain crack-tip passive films.[51–53, 65–70] Low-amplitude cyclic loading at stress ranges insufficient for cyclic-damage accumulation to dominate (e.g., below the ΔK_TH) have been referred to as ripple loads.[70] The influence of time-dependent cracking susceptibility on such ripple loads varies between different steels: Ford reports that stainless steel 304 is highly susceptible to ripple-load effects,[51] whereas Pao reports 4340 to be essentially immune.[49] These dependencies and trends as they relate to Custom 465 are not known.

Several of the current experimental findings are consistent with a mechanism that is governed by cyclic loading-induced rupture of the crack-tip film, thereby enabling enhanced H generation and

uptake to facilitate H-induced, time-dependent, IG-SCC failure. First, the results of the K-shed experiments in Figs. 3 and 4 demonstrate the dominance of transgranular cycle-dependent crack growth at high ΔK, whereas the time-dependent IG-SCC behavior occurs only during low-amplitude cyclic loading. This behavior is consistent with the ripple-load paradigm and is an important result in its own right.

Second, at intermediate levels of cyclic loading (but still below the quasi-static K_{ISCC}) the failure mode would be postulated to be a competition between a cycle-dependent damage accumulation mechanism and the ripple load-induced time-dependent IG-SCC cracking. In this paradigm, both failure mechanisms would contribute to the overall damage rate as per classic superposition models.[34] This expectation is realized in Fig. 6, where for a constant K_{max}, the lower $R = 0.5$ (thus, higher ΔK) testing show faster growth rates, and the fracture surface exhibits both an IG and transgranular morphology.

Third, Fig. 6 shows that for a constant ΔK, the cyclic loading-induced IG-SCC rates decrease with decreasing K_{max} (thus, decreasing R). In the film rupture paradigm, the crack-tip strain rate (ε'_{tip}) sets the time between rupture events at the crack tip (t_{rup}); as such, the degree of environmentally induced crack-growth enhancement is established by the interplay between the ε'_{tip} and the repassivation rate of the crack-tip film.[61, 65] The exact form of the equation used to calculate the ε'_{tip} is controversial;[24, 71] however, both empirically and mechanistically based models either explicitly or implicitly demonstrate (for a constant ΔK and f) that ε'_{tip} will decrease with decreasing R.[71] As such, the decrease in da/dt with R (and K_{max}) in Fig. 6 is fully consistent with lower expected ε'_{ip}, resulting in slower crack-tip film rupture relative to the repassivation rate. In addition, the extent and duration of exposure of the crack-tip surfaces would be decreased with decreasing R, which would result in the retardation of the observed da/dt. This is consistent with prior research that shows that at constant ΔK and f, da/dt resulting from ripple load-induced SCC will decrease with decreasing R.[51, 72]

Practical implications

Although the mechanistic underpinnings governing the observed time-dependent IG-SCC behavior well below the quasi-static K_{ISCC} were discussed in the preceding sections, it is important to also consider the engineering scale implications of these data. Prior efforts have noted the importance of considering such ripple-load effects when establishing the SCC susceptibility of materials operating in environments, where there may be superimposed cyclic and static loads.[50, 51] Such behavior is of particular relevance for high-strength precipitation-hardened martensitic stainless steels used in aerospace applications, where operational components are subject to a damaging combination of salt containing atmospheric environments, static loading, and cyclic/vibratory loading. It is critical to ensure that the testing protocols establishing the SCC susceptibility metrics for materials selection and structural health monitoring rigorously reflect the in-service mechanical loading conditions. This motivates more detailed work

Table 1. Composition of Custom 465

Custom 465 composition																
Fe	Cr	Ni	Co	Mo	W	V	Ti	Al	Si	Mn	S	P	As	Sn	Sb	La	Ce
Balance	11.4	10.9	0.1	0.9	0.7	—	1.6	0.1	65	150	5	18	19	9	6	<1	<1
wt %									wppm								

Bulk measurements (wt %) of Cr, Ni, Co, Mo, W, V, Ti, and Al were obtained via combustion infrared absorption. Bulk measurements of C (wt%) were obtained via ICP-AES or IC, and trace element analysis (wppm) of Si, Mn, S, P, As, Sn, Sb, La, and Ce were obtained via GDMS.

The interaction of corrosion fatigue and SCC
JR Donahue et al.

npj

7

to improve the fidelity of ε'_{tip} calculations, quantify the crack-tip repassivation kinetics in relevant crack-tip environments, explore the transient effect of different loading hold times, and potentially integrate this important behavior into the classic superposition models of environmental cracking.

In conclusion, fracture mechanics-based testing quantified the SCC and corrosion fatigue behavior of a precipitation-hardened martensitic stainless steel (Custom 465-H950) in full immersion [Cl⁻]-containing environments at various applied electrochemical potentials. The following conclusions were established:

- A plateau in the cycle-based crack-growth kinetics (da/dN) was observed during fatigue loading at low ΔK and [Cl⁻] levels above 0.6 M.
- Systematic evaluation of the fracture morphology and frequency dependence associated with plateau behavior demonstrated an intergranular morphology and constant time-dependent growth rates. These data strongly support a controlling SCC mechanism that is occurring well below the K_{ISCC} established for quasi-static loading.
- Low-amplitude cyclic loading below ΔK_{TH} (i.e. "ripple loads") are posited to enable time-dependent IG-SCC to occur below the K_{ISCC} via mechanical rupturing of the crack-tip film and enhancement of the H embrittlement-based SCC mechanism.

METHODS

Testing was performed on specimens excised from a 19.05 mm diameter bar of Custom 465 with a bulk and trace element compositions reported in Table 1, the former measured by inductively coupled plasma optical emission spectroscopy (ICP-OES) or infrared combustion (IC) and the latter by glow discharge mass spectroscopy (GDMS). The material was aged to the H950 condition (510 °C aging temperature) with a yield strength (σ_{ys}) of 1827 MPa, Ramberg-Osgood hardening parameters of $a = 0.13$–0.15 and $n = 23$–35, and a plain strain fracture toughness (K_{IC}) of 95 MPa$\sqrt{m}$ (reported by the manufacturer[73]). The microstructure is predominately tempered martensite that is precipitation-hardened via rod-shaped, nano-scale (10–50 nm) hexagonal phase (Ni₃Ti; η-phase).[73–77] Further details of the microstructure are reported in a companion study[13] that investigated the same lot of material. Fracture mechanics testing is performed on freely-rotating single edge notch (SEN) specimens with a rectangular-reduced gauge section with a width of 10.16 ± 0.13 mm, a thickness of 2.67 ± 0.05 mm, and a length of 35 ± 0.50 mm. A slow-grind final machining process was used to impart an initial 0.51 ± 0.03 mm deep notch with a 0.51 ± 0.03 mm opening that was centered in the reduced gauge.

For all testing, crack length was continuously monitored via dcPD[78, 79] using a 4 A current. The voltage was monitored via alumel wires (0.13 mm) symmetrically welded 0.5 and 17.5 mm from the notch center to collect active and reference potential readings, respectively. Johnson's equation for single edge cracks converts the potential signal to a real-time measurement of crack length (a). This active crack length monitoring enables K-control testing via software-controlled servo-hydraulic loading frames. Two broad types of testing were performed on separate SEN samples: (1) slow-rising displacement testing to characterize SCC behavior, and (2) cyclic loading under a constant K_{max}-decreasing ΔK (K-shed) protocol.

Regarding SCC testing, the specimens were first fatigue pre-cracked at a stress-ratio (R) of 0.1 with K_{max} falling from 15 to 8 MPa$\sqrt{m}$ at a final notch plus crack length of 0.8 mm. Slow-rising displacement testing (0.0003 mm/min) was then used to characterize the SCC properties in 0.6 M NaCl at a polarizations of −200 and −550 mV$_{SCE}$ (OCP was measured to be ≈−220 mV$_{SCE}$). This loading rate resulted in a dK/dt rate of 1 MPa$\sqrt{m}$/h prior to the onset of cracking, which increased with crack growth. Further details of this method are presented elsewhere.[48] Regarding the K-shed cyclic loading (sinusoidal waveform), the notched SEN specimens were first cyclically loaded at a maximum stress (σ_{max}) of 300 MPa, R of 0.5, and a frequency (f) of 2 Hz to form a crack. The ΔK increased with crack extension (at constant $\Delta\sigma$) up to 27.5 MPa$\sqrt{m}$ (thus, a K_{max} of 55 MPa$\sqrt{m}$). Once a K_{max} of 55 MPa$\sqrt{m}$ was achieved, a decreasing ΔK protocol with a constant K_{max} of 55 MPa$\sqrt{m}$ and a C-value of −0.4 mm⁻¹ (termed, K-shed protocol) was run until either a minimum da/dN of 10⁻⁸ mm/cycle or a ΔK of 2 MPa$\sqrt{m}$ was observed. Testing was performed in high humidity (RH > 90%) nitrogen, distilled water, or unbuffered NaCl solutions ranging from

0.0006 to 3 M. Electrochemical parameters are controlled through a potentiostat operating in floating ground mode with the specimen grounded through the frame grips. A standard calomel reference electrode is used and the specimen is surrounded by a platinum mesh ring to serve as a counter electrode. For cyclic loading, the potential was fixed at either −200 or −550 mV$_{SCE}$. The environment was maintained in a 500 ml chamber attached to the specimen and aerated electrolyte solutions were circulated using a peristaltic pump from 1 l reservoir at a rate of 20 ml/min. The growth rates (either da/dN or da/dt) are calculated via the secant method.[80] For all testing, post-test crack length averages were calculated from 10 measurements along the crack front. Variation between dcPD and measured values did not exceed 5%.

AUTHOR CONTRIBUTIONS
J.R.D. performed the experimental work, data analysis, and contributed to the authorship of this work. A.B.L. contributed to the experimental process and data generation. J.T.B. served as the principal investigator, conceived the research program, advised the experimental process, and was the primary author. In addition, he is the guarantor of this publication.

ADDITIONAL INFORMATION
Competing interests: The authors declare that they have no competing financial interests.

REFERENCES
1. Hyatt, M., Caton, R. & Lovell, D. Advanced materials development in commercial aircraft. In *Aircraft Design and Operations Conference, Seattle, WA* (American Institute of Aeronautics and Astronautics, 1989).
2. Lovell, D. & Disotell, M. Structural material trends in commercial aircraft. In *Conference on Air Transportation: Technical Perspectives and Forecasts* (American Institute of Aeronautics and Astronautics, 1978).
3. Hale, J. Boeing 787: From the ground up. *Aeromagazine* **4**, 17–24 (2006).
4. Leygraf, C. & Graedel, T. E. *Atmospheric Corrosion* (Wiley, 2000).
5. Schindelholz, E. & Kelly, R. G. Wetting phenomena and time of wetness in atmospheric corrosion: a review. *Corr. Rev.* **30**, 135–170 (2012).
6. Chen, Z. Y., Cui, F. & Kelly, R. G. An analytical modleing method for calculating the current delivery capacity of a thin-film cathode and the stability of localized corrosion under atmospheric environments. *ECS Trans.* **3**, 443–457 (2007).
7. Lizlovs, E. A. & Bond, A. P. Anodic polarization behavior of high-purity 13 and 18% Cr stainless steels. *J. Electrochem. Soc.* **122**, 719–722 (1975).
8. Ilevbare, G. O. & Burstein, G. T. The role of alloyed molybdenum in the inhibition of pitting corrosion in stainless steels. *Corr. Sci.* **43**, 485–513 (2001).
9. Ebara, R. Corrosion fatigue crack initiation behavior of stainless steels. *Proc. Eng.* **2**, 1297–1306 (2010).
10. Syrett, B. C., Viswanathan, R., Wing, S. S. & Wittig, J. E. Effect of microstructure on pitting and corrosion fatigue of 17-4 PH turbine blade steel in chloride environments. *Corrosion* **38**, 273–282 (1982).
11. Akid, R. in *Effects of the Environment on the Initiation of Crack Growth, ASTM STP 1298* (eds Van Der Sluys, W. A., Piascik, R. S., & Zawierucha, R.) 3–17 (ASTM, 1997).
12. Turnbull, A. in *Comprehensive Structural Integrity* (eds Milne, I., Ritchie, R. O., & Karihaloo, B. L.) 163–210 (Elsevier, Ltd., 2003).
13. Donahue, J. R. & Burns, J. T. Effect of chloride concentration on the corrosion-fatigue crack behavior of an age-hardenable martensitic stainless steel. *Int. J. Fatigue* **91**, 79–99 (2016).
14. Hata, S., Nagai, N., Yasui, T. & Tsukamoto, H. Investigation of corrosion fatigue phenomena in transient zone and preventive coating and blade design against fouling and corrosive environment for mechanical drive turbines. *Int. J. Fluid Mach. Syst.* **1**, 121–139 (2008).
15. Perkins, K. M. & Bache, M. R. Corrosion fatigue of a 12%Cr low pressure turbine blade steel in simulated service environments. *Int. J. Fatigue* **27**, 1499–1508 (2005).

npj

The interaction of corrosion fatigue and SCC
JR Donahue et al.

8

16. Lin, C. K., Fan, W. C. & Tsai, W. J. Corrosion fatigue of precipitation-hardening martensitic stainless steel. *Corrosion* **58**, 904–911 (2002).

17. Bhambri, S. K. Intergranular fracture in 13 wt% chromium martensitic stainless steel. *J. Mat. Sci.* **21**, 1741–1746 (1986).

18. Islam, M., Campbell, G. & Hsu, R. Fatigue and tensile properties of EB welded 17-4 PH steel—evaluation shows that EBW resulted in minimal loss in tensile strength. *Weld. J.* **68**, 45–50 (1989).

19. Rhouma, A. B., Sidhom, H., Braham, C., Lédion, J. & Fitzpatrick, M. E. Effects of surface preparation on pitting resistance, residual stress, and stress corrosion cracking in austenitic stainless steels. *J. Mat. Eng. Perf.* **10**, 507–514 (2001).

20. Ebara, R., Kai, T. & Inoue, K. in *Corrosion Fatigue Technology* (eds Craig, H. L., Crooker, T. W., Hoeppner, D.W.) 155–168 (ASTM, 1978).

21. Lee, E. U., Goswami, R., Jones, M. & Vasudevan, A. K. Environment-assisted cracking in Custom 465 stainless steel. *Met. Mat. Trans. A* **42A**, 415–423 (2011).

22. Akita, M., Nakajima, M., Tokaji, K. & Shimizu, T. Fatigue crack propagation of 444 stainless steel welded joints in air and in 3%NaCl aqueous solution. *Mat. Des.* **27**, 92–99 (2006).

23. Slifka, A. J. et al. Fatigue crack growth of two pipeline steels in a pressurized hydrogen environment. *Corr. Sci.* **78**, 313–321 (2013).

24. Gangloff, R. P. in *Environment Induced Cracking of Metals* (eds Gangloff, R. P. & Ives, M. B.) 55–109 (NACE, 1990).

25. Lin, C. K. & Tsai, W. J. Corrosion fatigue behaviour of a 15Cr-6Ni precipitation-hardening stainless steel in different tempers. *Fatigue Fail. Eng. Mater. Str.* **23**, 489–497 (2000).

26. Logsdon, W. A. An evaluation of the crack growth and fracture properties of AISI 403 modified 12 Cr stainless steel. *Eng. Frac. Mech.* **7**, 23–40 (1975).

27. Gangloff, R. P. Crack size effects on the chemical driving force for aqueous corrosion fatigue. *Met. Trans. A* **16**, 953–969 (1985).

28. Pioszak, G. *Hydrogen Assisted Cracking of Ultra-high Strength Steels*. PhD thesis, University of Virginia (2015).

29. Schaller, R. *Local Probe Techniques for Hydrogen Measurement in Ultra-High Strength Steels*. PhD thesis, University of Virginia (2016).

30. Schaller, R. F. & Scully, J. R. Spatial determination of diffusible hydrogen concentrations proximate to pits in a Fe-Cr-Ni-Mo steel using the Scanning Kelvin Probe. *Electrochem. Commun.* **63**, 5–9 (2016).

31. Wei, R. P. & Gao, M. Reconsideration of the superposition model for environmentally assisted fatigue crack growth. *Scr. Met.* **17**, 959–962 (1983).

32. Wei, R. P. Environmental considerations for fatigue cracking. *Fatigue Fail. Eng. Mater. Str.* **25**, 845–854 (2002).

33. Wei, R. P. & Landes, J. D. Correlation between sustained-load and fatigue crack growth in high-strength steel. *Mater. Res. Std.* **9**, 25–28 (1969).

34. McEvily, A. J. & Wei, R. P. in *Corrosion Fatigue: Chemistry, Mechanics, and Microstructure, NACE-2* (eds McEvily, A. J. & Staehle, R. W.) 381–395 (NACE, 1972).

35. Lynch, S. Hydrogen embrittlement phenomena and mechanisms. *Corr. Rev.* **30**, 105–123 (2012).

36. Thomas, S., Sundararajan, G., White, P. D. & Birbilis, N. The effect of absorbed hydrogen on the corrosion of steels: review, discussion, and implications. *Corrosion* **73**, 426–436 (2017).

37. Gangloff, R. P., Ha, H., Burns, J. T. & Scully, J. R. Measurement and modeling of hydrogen environment assisted cracking in Monel K-500. *Met. Mater. Trans. A* **45A**, 3814–3834 (2014).

38. Kalnaus, S., Zhang, J. & Jiang, Y. Stress-corrosion cracking of AISI 4340 steel in aqueous environments. *Met. Trans. A* **42**, 434–447 (2011).

39. Weng, L., Zhang, J. X., Kalnaus, S., Feng, M. L. & Jiang, Y. Y. Corrosion fatigue crack growth of AISI 4340 steel. *Int. J. Fatigue* **48**, 156–164 (2013).

40. Li, D. M., Gangloff, R. P. & Scully, J. R. Hydrogen trap states in ultrahigh-strength AERMET 100 steel. *Met. Mater. Trans. A* **35A**, 849–864 (2004).

41. Harris, Z. D. et al. The effect of microstructural variation on the hydrogen environment-assisted cracking of Monel K-500. *Met. Mater. Trans. A* **47**, 3488–3510 (2016).

42. Gangloff, R. P. in *Comprehensive Structural Integrity* Vol. 6 (eds Milne, I., Ritchie, R. O., & Karihaloo, B.) 31–101 (Elsevier Science, 2003).

43. Sandoz, G., FuJii, C. T. & Brown, B. F. Solution chemistry within stress-corrosion cracks in alloy steels. *Corr. Sci.* **10**, 839 (1970).

44. Brown, B. F., Fujii, C. T. & Dahlberg, E. P. Methods for studying the solution chemistry within stress corrosion cracks. *J. ECS* **116**, 218–219 (1969).

45. Smith, J. A., Peterson, M. H. & Brown, B. F. Electrochemical conditions at tip of an advancing stress corrosion crack in AISI-4340 steel. *Corrosion* **26**, 539 (1970).

46. Turnbull, A. & Thomas, J. G. N. A model of crack electrochemistry for steels in the active state based on mass transport by diffusion and ion migration. *J. Electrochem. Soc.* **129**, 1412–1422 (1982).

47. Andresen, P. L. & Young, L. M. in *7th Environmental Degradation of Materials In Nuclear Power Systems* 579–596 (NACE, 1995).

48. Pioszak, G. & Gangloff, R. P. Hydrogen environment assisted cracking of a modern ultra-high strength martensitic stainless steel. *Corrosion* **73**, 1132–1156 (2017).

49. Pao, P. S., Bayles, R. A. & Yoder, G. R. Effect of ripple load on stress-corrosion cracking in structural steels. *J. Eng. Mater. Technol.* **113**, 125–129 (1991).

50. Crooker, T. & Hauser, J. *A Literature Review on the Influence of Small-amplitude Cyclic Loading on Stress-Corrosion Cracking in Alloys* (DTIC Document, 1986).

51. Ford, F. & Silverman, M. Effect of loading rate on environmentally controlled cracking of sensitized 304 stainless steel in high purity water. *Corrosion* **36**, 597–603 (1980).

52. Mendoza, J. A. & Sykes, J. The effect of low-frequency cyclic stresses on the initiation of stress corrosion cracks in X60 line pipe steel in carbonate solutions. *Corr. Sci.* **23**, 547–558 (1983).

53. Parkins, R. N. & Greenwell, B. S. The interface between corrosion fatigue and stress-corrosion cracking. *Metal Sci.* **11**, 405–413, (1977).

54. Bayles, B. A., Pao, P. S., Gill, S. J. & Yoder, G. R. in *Systems Engineering Approach to Mechanical Failure Prevention* (eds Pusey, H. C. & Pusey, S. C.) 167–176 (Vibration Institute, 1993).

55. Horstmann, M. & Gregory, J. K. Observations on the ripple loading effect. *Scr. Met. Mater.* **25**, 2503–2506 (1991).

56. Wei, R., Shim, G., Tanaka, K. & Gangloff, R. Embrittlement by the localized crack environment 243–263 (*AIME*, 1984).

57. Turnbull, A. Theoretical analysis of influence of crack dimensions and geometry on mass-transport in corrosion-fatigue cracks. *Mater. Sci. Technol.* **1**, 700–710 (1985).

58. Turnbull, A. & Ferriss, D. H. Mathematical modeling of the electrochemistry in corrosion fatigue cracks in steel corroding in marine environments. *Corr. Sci.* **27**, 1323–1350 (1987).

59. Scully, J. R. & Moran, P. J. Influence of strain on the environmental hydrogen-assisted cracking of a high-strength steel in sodium-chloride solution. *Corrosion* **44**, 176–185 (1988).

60. Scully, J. R. & Moran, P. J. The influence of strain on hydrogen entry and transport in a high-strength steel in sodium-chloride solution. *J. Electrochem. Soc.* **135**, 1337–1348 (1988).

61. Scully, J. C. The interaction of strain-rate and repassivation rate in stress-corrosion crack-propagation. *Corr. Sci.* **20**, 997–1016 (1980).

62. Madden, S. B., Moosbauer, D. J. & Scully, J. R. Effects of chromate and molybdate ions on scratch repassivation behavior of precipitation hardened aluminum alloys. *ECS Trans.* **50**, 57–78 (2013).

63. Ford, F. P. in *Environment Induced Cracking of Metals* (eds Gangloff, R. P. & Ives, M. B.) 139–166 (NACE, 1990).

64. Somerday, B. P., Young, L. M. & Gangloff, R. P. Crack tip mechanics effects on environment-assisted cracking of beta-titanium alloys in aqueous NaCl. *Fatigue Fail. Eng. Mater. Str.* **23**, 39–58 (2000).

65. Warner, J. S. & Gangloff, R. P. Alloy induced inhibition of fatigue crack growth in age-hardenable Al-Cu Alloys. *Int. J. Fatigue* **42**, 35–44 (2012).

66. Warner, J. S. & Gangloff, R. P. Molybdate inhibition of corrosion fatigue crack propagation in precipitation hardened Al-Cu-Li. *Corr. Sci.* **62**, 11–21 (2012).

67. Liu, X. F., Huang, S. J. & Gu, H. C. The effect of corrosion inhibiting pigments on environmentally assisted cracking of high strength aluminum alloy. *Corr. Sci.* **45**, 1921–1938 (2003).

68. Gasem, Z. M. & Gangloff, R. P. in *Chemistry and electrochemistry of corrosion and stress corrosion cracking: a symposium honoring the contributions of R.W. Staehle* (ed Jones, R. H.) 501–521 (TMS-AIME, 2001).

69. Dawson, D. B. & Pelloux, R. M. Corrosion fatigue crack growth of titanium-alloys in aqueous environments. *Met. Trans.* **5**, 723–731 (1974).

70. Fessler, R. R. & Barlo, T. J. *Threshold-Stress Determination Using Tapered Specimens and Cyclic Stresses* 368–382 (ASTM International, 1984).

71. Ford, F. P. Status of research on environmentally assisted cracking in LWR pressure vessel steels. *J. Pres. Ves. Technol.* **110**, 113–128 (1988).

72. Shoji, T., Aiyama, S., Takahashi, H. & Suzuki, M. Effects of stress intensity rate K and stress ratio R on corrosion fatigue crack growth enhancement below KISCC. *Corrosion* **34**, 276–282 (1978).

73. Carpenter. *Custom 465 Stainless—Techical Datasheet*. http://cartech.ides.com/datasheet.aspx?i=103&e=55 (2013).

74. Garrison, W. M. Jr. Ultrahigh-strength steels for aerospace applications. *J. Mater.* **42**, 20–24 (1990).

75. Sedriks, A. J. *Corrosion of Stainless Steel* 2nd edn. (Wiley, 1996).

76. Grujicic, M., Tangrila, S., Cavin, O. B., Porter, W. D. & Hubbard, C. R. Effect of iron additions on structure of Laves phases in Nb-Cr-Fe alloys. *Mater. Sci. Eng. A* **160**, 37–48 (1993).

77. Hochanadel, P. W., Edwards, G. R., Robino, C. V. & Cieslak, M. J. Heat treatment of investment cast PH 13-8 Mo stainless steel: part I. Mechanical properties and microstructure. *Met. Mater. Trans. A* **25**, 789–798 (1994).

The interaction of corrosion fatigue and SCC
JR Donahue et al.

9

78. Gangloff, R. P., Slavik, D. C., Piascik, R. S. & Van Stone, R. H. *Direct Current Electrical Potential Measurement of the Growth of Small Cracks* 116–168 (STP, 1992).

79. Donald, J. K. & Ruschau, J. in *Fatigue Crack Measurement: Techniques and Applications* (eds Marsh, K. J., Smith, R. A., & Ritchie, R. O.) 11–37 (Engineering Materials Advisory Service, 1991).

80. ASTM. *ASTM E647-15e1: Standard Test Method for Measurement of Fatigue Crack Growth Rates* (ASTM International, 2015).